Vision, Modeling, and Visualization (2022)
J. Bender, M. Botsch, and D. Keim (Eds.)

Alignment and Reassembly of Broken Specimens for Creep Ductility Measurements

Volker Knauthe[1†], Maurice Kraus[1†], Max von Buelow[1], Tristan Wirth[1], Arne Rak[1,4], Laurenz Merth[1], Alexander Erbe[3], Christian Kontermann[3], Stefan Guthe[1], Arjan Kuijper[2] and Dieter W. Fellner[1,2,5]

[1]Technical University of Darmstadt, Interactive Graphics Systems Group, Germany [2]Fraunhofer IGD, Germany
[3]TU Darmstadt, Institute for Materials Technology [4]TU Darmstadt, Numerical Methods in Mechanical Engineering
[5]Graz University of Technology, Institute of Computer Graphics and Knowledge Visualization, Austria

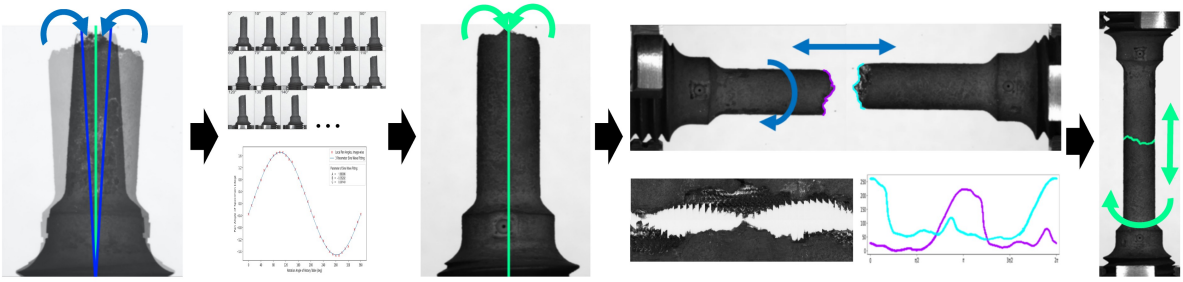

Figure 1: *This image shows our alignment and reassembling pipeline for broken specimens used to assess creep ductility measurements. As an input, we receive two series of images, each containing horizontally rotated viewpoints of a specimen half. However, due to mechanical constraints, those are tilted (blue axis lines) compared to the rotation axis of their mounting (green axis lines). We correct this tilting in each image with an axis fitting approach utilizing sinusoidal skew behavior. In a next step, we extract features from the specimen break points and optimize a rotation and translation function to obtain an image state approximating a whole specimen shortly before the breaking point. Those images are then used for a space carving approach and subsequently specimen characteristic extraction.*

Abstract

Designing new types of heat-resistant steel components is an important and active research field in material science. It requires detailed knowledge of the inherent steel properties, especially concerning their creep ductility. Highly precise automatic state-of-the-art approaches for such measurements are very expensive and often times invasive. The alternative requires manual work from specialists and is time consuming and unrobust. In this paper, we present a novel approach that uses a photometric scanning system for capturing the geometry of steel specimens, making further measurement extractions possible. In our proposed system, we apply calibration for pan angles that occur during capturing and a robust reassembly for matching two broken specimen pieces to extract the specimen's geometry. We compare our results against μCT scans and found that it deviates by 0.057 mm on average distributed over the whole specimen for a small amount of 36 captured images. Additionally, comparisons to manually measured values indicate that our system leads to more robust measurements.

CCS Concepts

• ***Computing methodologies*** → *Shape analysis;* • ***Applied computing*** → ***Engineering;***

1. Introduction

Constructing modern steel components with heat resistance properties requires precise knowledge of specific key material characteristics. An important criterion is crack resistance, which is derived from creep ductility properties. These properties facilitate the distribution of stress peaks in critical areas [AB83].
Ductility is measured using experiments where steel specimens are set up in multi-specimen creep test rigs. These rigs put temperatures of 400 °C to 850 °C and tension up to 600 MPa on each specimen [WWAG88; KGK87; KSK12]. After fixed durations, specimens are taken out of their rigs to be scanned by an automated image based

† equivalent contribution

DOI: 10.2312/vmv.20221201

capturing setup with a measuring accuracy of 10 µm. This device is illustrated in fig. 2. The images are used to create 3D reconstructions of the specimen, which are then used to assess creep ductility properties. After up to 100 000 h, a specimen will break into two pieces ending an experiment. The broken half of a specimen as well as an assembled specimen can be seen in fig. 1 The interpretation of ductility parameters can be done by assessing the *uniform elongation* value that is derived from a specimen's elongation and necking over the course of an experiment and after the specimen is broken.
While the existing measurement system yields good initial results, we identified two strategies to further improve the current accuracy and robustness. First, manually mounting a specimen perpendicular to the camera usually leads to a mounting error. The reason for this is that humans do not have the capabilities to operate in a micrometer scope. Furthermore, due to the heating process, material warping will hinder specimen fastening. This leads to a skewed specimen position. This results in images where the specimen axis is misaligned in comparison to the turn-table axis. We propose an algorithm that utilizes the detection of specimen angles, as well as the turn-table angle to correct the alignment in the captured image information.
Second, when a specimen breaks, the original process was to manually combine the two parts and measure them as a whole specimen. This however requires an experienced engineer and, in addition, this usually does not lead to reproducible measurements. Furthermore, manual fitting strategies are often times an invasive process. We introduce a novel image based edge fitting algorithm that uses a parameter-less approach to virtually reassemble broken specimen halves in a robust manner, improving the fitting accuracy and robustness of the overall reconstruction.
While both algorithms are optimized for this special use case, they can be generalized to work with any cylindrical shape.

In summary our contributions are:

- A deterministic, parameter-less, robust pipeline for high precision reassembly and reconstruction of broken specimens.
- A post-scan calibration for pan angle correction in images.
- A non-invasive and cost/time effective capturing process, with an accuracy comparable to μCT measurements.

2. Related Work

The images used in this work are obtained through an orthographic scanning setup [KvBG*21]. This setup uses a rotary table for specimen mounting, a lab jack with a CMOS camera and a telecentric lens to capture images, as illustrated in fig. 2. Furthermore, there are two possible lighting setups, one that facilitates clear images of the specimen surface and one that enables silhouette images with a high capturing quality, especially in the region of a specimen edges. The specimens that are scanned in the provided setup are always cylindrical (cf. fig. 1). Furthermore, they contain two round ceramic measurement markers, one on each end, on the front and back side [AB83].

Our reconstruction approach is primarily based on the shape-from-silhouette method [Bau74; AA20] which is well suited for the rotary table setup. Methods for silhouette extractions are widely researched and favor a highly controlled background, which we can

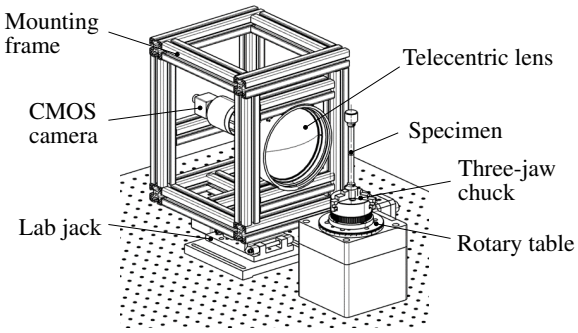

Figure 2: *Scanning setup for steel specimen [KvBG*21].*

provide [Pic04; CBK04; McI00; EHD00; KSK*07; SAT06]. Those extractions are used to create visual hulls [Lau94; MBR*00; Sch21] of a specimen, using a space carving approach [KS99; MYA03].
The correction of rotation axes was not yet used for high precision steel specimen evaluation task, but similar approaches have been used in archaeology, for pottery reconstruction, and for a similar rotation table setups [KSM05; MYA03]. The specimen rotation leads to a sine wave pattern, and we can therefore utilize a sine wave fitting method to calculate the maximal skew [Han00; AH03].
Our reassembling approach utilizes feature extraction based on edge detection methods to identify and match fragment break points, that originate from archaeological reassembling processes [MK03; EDDP20; RN14]. Alternatively, there are 3D geometry based approaches for mesh matching [SLLL17; LGZ20]. However, we can not use a 3D approach, as we can not capture a high quality mesh of the edge, due to camera position constraints. To find the original orientation of two broken specimen parts, a registration process is needed. This can be done with using the Euclidean distance as error metric for broken pottery assembling [KS04], or by utilizing a non-linear regression to fit a polynomial function for an edge [RN14]. The most frequently used approach to reassemble broken objects in the form of 3D meshes or point clouds is the iterative closest point algorithm, which is used to find a transformation to align two sets of points optimally [WC04; ZYM*15; PJ17; Sak19]. A reasonable initial estimate can be used to avoid local minima [PK03; LGZ20]. While several subroutines of the proposed system have been discussed in previous work, to our knowledge there is no system that utilizes these procedures for the virtual reassembly of high precision scans of steel specimens.

3. Specimen Reassembly

We propose a pipeline that relies on images captured with the previously presented scanning system (section 2). These images are captured uniformly in a defined rotational step size α around the object (i.e. full 360°). Our pipeline for specimen reassembly then coarsely follows fig. 1: First, section 3.1 describes the calibration that extracts the pan angle from the set of specimen images, followed by the alignment process for two broken specimen parts in section 3.2. Finally, section 3.1 describes the extraction of the specimen point cloud.

3.1. Pan Angle Calibration

The initial step for our reassembly system is calibration. Since there is no trivial mechanical approach to mount arbitrary specimens on a turntable in a way that their rotation axis is aligned with the rotation axis of the turntable, we introduce a preprocessing step aimed at correcting the input images as if their rotation axis would be aligned. Therefore, we assume the basic shape of the major part of the specimen—excluding the shaft for mounting and the fracture edge—to be an inclined circular cylinder. Based on this assumption, the object axis is defined as the ray through the centers of the two circular surfaces of the cylinder. Subsequently, the specimen pan angle is defined as the angle between object axis and rotation axis of the rotary table. Our approach for image-wise determination of the object axes is based on the specimen contour. Due to the environmental lighting conditions of the setup, contour extraction from strong brightness changes in boundary areas of the specimen is straightforward. The object axis in camera coordinates is then determined as a linear function that minimizes the squared distance to the left and right contour edges. The rotation axis of the rotary table corresponds to the reflection axis of the object axes in two images with a rotary angle difference of 180°. Due to the camera's and rotary table's static positioning, the rotation axis is static in the images and usually close to 0°, since the rotation along the viewing direction is fixed by design. To minimize errors in the rotary table axis calculation, our system averages over the reflection axis from all images. Our system then determines the pan angle of the specimen image-wise using the object axes and the rotation axis. The consideration of rotation matrix and projection matrix (parallel projection) indicates that a sinusoidal wave-shaped correlation of the pan angles exists in the images due to the projection from 3D into 2D space. This characteristic is used for a global optimization of the pan angle determination in terms of a three parameter sine wave fitting [AH03] making estimated pan angle more robust.

Our system applies two corrections per image based on the global pan angle representation. The first correction corresponds to a rotation of the image parallel to the image plane by the pan angle of the specimen in the image. This correction aligns all specimen views with the rotation axis of the rotary table. The second correction represents a rotation of the image orthogonal to the image plane by the pan angle of the specimen for a rotary angle difference of 90°. This distortion corrects the error regarding the length of the specimen due to the inclination into the image plane and is only useful for very small pan angles, as for larger pan angles the features of the specimen will be distorted. In both cases, the center of rotation is determined as the intersection of the corresponding object axis and the rotation axis.

Given the set of corrected images, we are able to safely proceed with the following processing step of aligning specimen parts.

3.2. Alignment

Break Point Edge Extraction The registration process starts with a feature extraction step that analyses broken specimens' break point edges. Therefore, our system leverages the cylindrical shape of the specimen parts to unroll their surface onto a panorama plane P_δ as follows in order to apply succeeding photometric consistency checks:

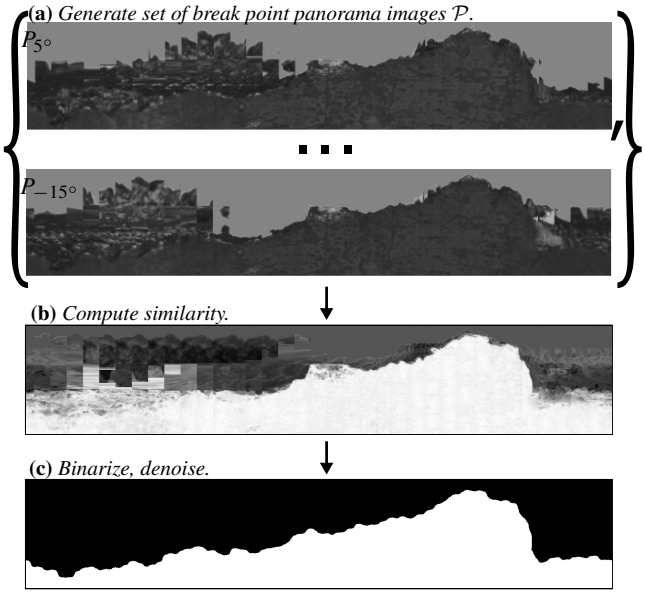

Figure 3: *Steps involved in extracting break point edge of a broken specimen part.*

Every panorama consists of the concatenation of flattened chunks from the set of images. The position of the extraction region remains static in camera coordinates across images. As the object rotates, concatenating the same projected region across images effectively unrolls the specimen. The parameter δ further defines the offset angle representing the overall angular position of the chunk. Figure 3a shows two break point panoramas with different offsets δ for the same specimen. In the foreground of the images, the specimen's gage section surface is visible, which is aligned in both panoramas and therefore has a constant appearance. The background shows the break point surface, which, however, differs in appearance between $P_{5°}$ and $P_{-15°}$. This is caused by the concavities in the break point surface effectively violating the cylindrical panorama projection, which result in different surface points being sampled for the same orthographic projections.

Our system calculates photometric consistency based on the set of available break point panorama images $\mathcal{P}$ extracted from different offsets in order to identify visual similarities between them. High similarity indicates a high probability that a pixel belongs to the gage section surface since the latter is always aligned and visible in the foreground of any panorama images. Therefore, our system computes the cumulative difference image C:

$$C = \sum_{(P_\delta, P_{\delta'}) \in \mathcal{P} \times \mathcal{P}} |P_\delta - P_{\delta'}| \tag{1}$$

Then, the cumulative difference image gets normalized and inverted, resulting in a similarity image as shown in fig. 3b. Pixels in the panorama that reach a certain threshold are then defined as the gage section. Additionally, we apply further denoising techniques using mathematical morphology in order to be able to directly derive the break point edge line from the processed panorama. The choice of threshold impacts the accuracy of the extracted break

point edge. Therefore, there is no optimal value that fits every specimen dataset. This especially applies to less controlled environments. Nevertheless, the actual registration process described in the following gives a strong indication about the threshold quality, making automatic threshold estimation possible.

Break Point Edge Registration We define the registration as the problem of finding a shared coordinate system for both sets of specimen images. The coordinate system of the first half is used as the global coordinate system, and a projection must be found that matches the break point edge of the second half. The projection consists of the rotation of the second specimen half along the Z-axis R_z, as well as its translation relative to the shared coordinate system T_z. To estimate the correct rotation R_z of the second break point edge, our system calculates the *circular cross-correlation* metric, which is a measure of similarity between two signals as a function of the displacement of one relative to the other [Wan19]. It is applied to two real finite discrete signals $x, h \in \mathbb{R}^n$ (i.e. the extracted break point edge):

$$(x * h)[m] = \sum_{i=0}^{n-1} x[i]h[(m+i)_{\bmod n}] \tag{2}$$

To find the optimal rotational correction R_z of the second break point edge, our system computes the displacement resulting in the highest circular cross-correlation. Finally, we determine the translation T_z of the displaced break point edge along the specimen's z-axis such that both break point edges coincide. Our processing system achieves this by minimizing the matching error $\varepsilon = \sum_i \log(1 + |d_i|)$ where d_i is the signed distance between the i^{th} points of the compared edges. We additionally use the minimum matching error ($\min\varepsilon$) as a quality metric for the overall registration process. This allows us, to optimize the process with respect to different extraction thresholds, eliminating the need for a fixed threshold.

3.3. Visual Hull Extraction

The corrected and aligned images are then used to determine the visual hull [Lau94] of the specimen. This is done by space carving [KS99], taking into account the parallel projection due to the orthographic camera. In this context, the object axis is aligned with the Z-axis, which is centered horizontally and traverses the discretized space vertically. This procedure ensures that the specimen or its visual hull is oriented orthogonally to the footprint of the space.

4. Results

In the following experiments and accompanying results, we use images acquired with the orthographic scanning setup [KvBG*21] where each image has the size of 5496×3672 and a single pixel corresponds to $8.5714\,\mu\text{m}$. In these experiments, we evaluate our proposed specimen reassembly pipeline. First, we evaluate the pan angle calibration on synthetic and a real specimen. This is followed by experiments for the presented alignment methods. Here, edge detection and registration are evaluated separately. Finally, the reconstruction is evaluated against real invasive micro computer tomography (μCT) scanned specimen and an outlook is given on the feasibility of determining the distance between two broken specimen pieces.

4.1. Pan Angle Calibration

To evaluate the orientation of the pan angle, we take images every 10° (θ_{10°), for a total of 36, to achieve a full 360° rotation. Figure 4 shows four exemplary images for such a set for a real specimen. This image series has a pan angle deviation of 3° with respect to the vertical image axis. The evaluation of the object axis is based on the assumption that the steel specimens have a cylindrical shape. From this, we derived that the axis is centered between the left and right edge of the silhouette at every point. Consequently, the distances from the axis to the left and right edge of the silhouette orthogonal to the axis are identical or in other words, their difference is zero. The actual average and maximum deviations in pixels between the true and determined object axis for a real and a synthetic specimen are denoted in the supplemental material.

The results for the synthetic specimen indicate that the average deviation of the determined object axis concerning the defined object axis, considering its entire image set, is significantly less than one pixel. Similarly, the maximum deviation of the determined object axis with respect to the real object axis is slightly greater than two pixels. Both values are very small in relation to the image resolution. For the real specimen, the overall deviation is higher, but this is as expected due to the less controlled environment. The average difference in the images is about 1.163 pixels. In contrast, there is an increase in the maximum difference to a value of about 16 pixels. This is caused by additional noise in the image and by the greater partial deformation of the cylinder lateral surface caused by the load test. Nevertheless, this illustrates that even with a real specimen, the overall average deviation per image, relative to the resolution of the images, is low.

Furthermore, we evaluate the correlation between the determined object's pan angle and the rotary table axis. We found that the pan angles for the synthetic specimen correspond to a cosine wave with an amplitude gain of -3.0. Comparing the local angles determined using the axes and the true angle plot indicates a maximum absolute difference of approximately 0.0046° between local and true angles. The comparison of the local pan angles with the true angle is given in the supplemental material.

4.2. Alignment

Break Point Edge Extraction Identical to the experiments regarding the pan angle alignment, we use multiple captures given by the rotary table setup with θ_{10°. To evaluate the significance of the number of captures for the edge detection, we additionally test with θ_{20° and θ_{30° and correspondingly less images.

Figure 5 illustrates the panorama image P_{-5° of a synthetic specimen for step size of θ_{10°. Thereby, the calculated break point edges for 10°, 20° and 30° are superimposed to allow for a visual comparison. The results indicate that although a step size of 30° suffices for the most part, it also imposes some inaccuracies, which can be seen at ① and ②. A similar result can be observed in fig. 6 and fig. 7. In the former one, some divergence of the detected edges

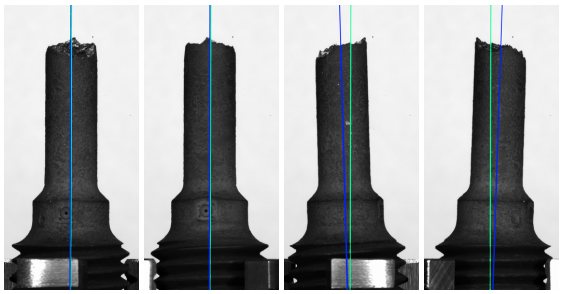

Figure 4: *Images of the real specimen with the global rotation angle of the turntable (blue) and the local specimen angle (teal). The first and second image have the maximum tilt into and against the camera (0° as baseline and 180° rotation). Furthermore, the ceramic measurement markers can be seen. The third and fourth image have the maximum tilt on the image axis (90° and 270°).*

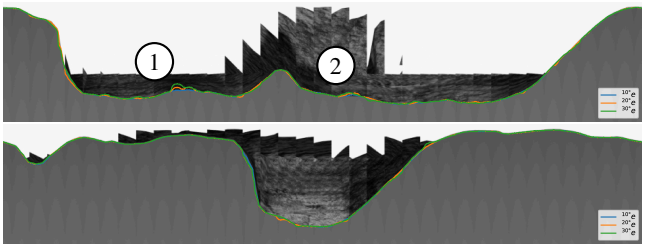

Figure 5: *Detected edges of the two halves of a 3D specimen at multiple step sizes. Some minor inaccuracies can be seen at (1) and (2), where 10° performs best.*

occurs at (1) where the gage section surface is particularly reflective. This causes gaps to open up during the morphological opening operation which are then closed with the edge repair algorithm, as recognizable by the straight lines around (1). A more severe error can be seen at (2) where the edge with step size 30° briefly diverges from 10° and 20° indicating that there is not enough information in the reduced amount of specimen images to distinguish the break point surface. In fig. 7 the specimen illustrated contains minor discrepancies at (1), (2) and (3). The area around (4) once more emphasizes the challenge with reflective surfaces, as this part of the break point is completely avoided by all three edges. This happens when some false negatives in the binarized similarity image caused by the reflective region are enlarged in the morphological opening

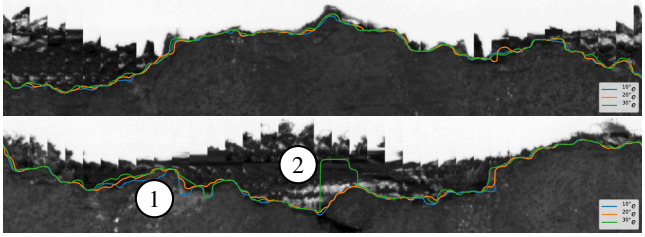

Figure 6: *Detected edges of a real specimen at multiple step sizes. Inaccuracies can be seen at (1) and (2), where 10° performs best.*

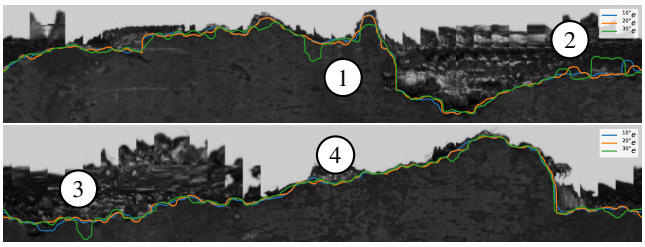

Figure 7: *Detected edges of a real specimen at multiple step sizes. Minor inaccuracies occur at (1), (2), and (3). (4) illustrates the challenge with reflective surfaces that result in avoiding the break point on all three edges*

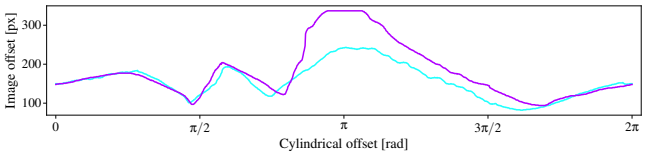

Figure 8: *Adjusted Real-3 specimen registered edges*

operation, in this case completely separating it from the gage section. The presented results justify the step size choice of $\theta_{10°}$. This is especially noteworthy from the perspective that both the alignment and the capturing time do not increase noticeably.

Break Point Edge Registration The successful match of two specimen halves requires matching the translation T and rotation R of two break point edges constrained through the binarization threshold t. Hereby, one specimen half needs to be rotated and translated before it is possible to reassemble them. Similar to the preceding experiments, we evaluate multiple θ_{step}. Table 1 depicts the performance of two synthetic and three real specimens and shows the respective ground truth data (if available) of the optimal translation and rotation. Furthermore, we provide the matching error ε and computed threshold.

The results for t indicate that a lower threshold is required for more complex geometries to achieve the smallest matching error. The most prominent differences in threshold values are observed for the *3D* and *Real-3* samples, which have the simplest and most complex geometries respectively. The results also show that there is no universal value for t that works well for all sample data sets. Instead, an optimal value for t must be determined individually for each sample, which is achieved by our registration algorithm. Moreover, the results show that our algorithm is able to approximate the exact rotational error R_z, which ranges from 174.51° to 174.75° for the *3D* specimen and from 174.26° to 174.51° for the *3D-skewed* specimen well. The matching error ε correlates primarily with the step size θ_{step}. Thus, an increasing step size leads to an increasing matching error. This observation confirms our findings from the preceding experiments, where we outlined that edges extracted at larger step sizes generally contain more noise and are therefore less accurate. Lastly, a notable result is that the matching error for a registration with manually adjusted edges for *Real-3*, is the highest of the experiments, even though the edges were

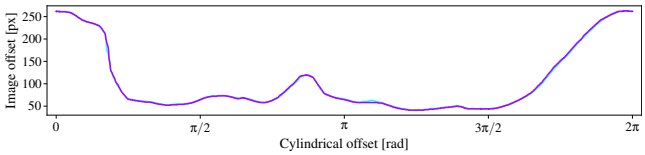

(a) *Registered edges of the 3D specimen.*

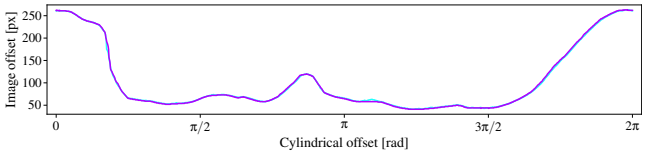

(b) *Registered edges of the 3D-skewed specimen.*

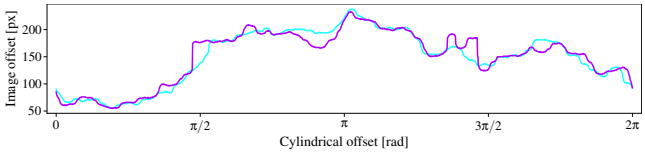

(c) *Registered edges of the Real-1 specimen.*

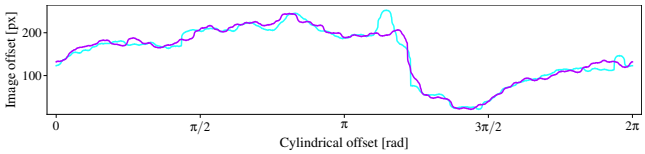

(d) *Registered edges of the Real-2 specimen.*

Figure 9: *Registered break point edges extracted with* θ_{10°.

modified to increase accuracy. This is due to a torn piece, which is situated at the large gap between the edges shown in fig. 8 and drastically increases the matching error. Nevertheless, we observe that our algorithm was able to successfully match the edges even in the absence of geometry on the opposite half. To check the validity of the other four specimens, we plotted the registered edges for θ_{10° in fig. 9. In doing so, we can see that our algorithm maps the synthetic specimens almost perfectly and even the real specimens with sufficient accuracy. In general, the error is more pronounced for real samples. This is due to the fact that a large amount of material degradation can occur as a result of the load tests, which causes that the edges cannot be positioned unambiguously on top of each other.

4.3. Visual Hull Extraction

Figure 10 shows a real specimen and the 3D model of the visual hull from the same viewpoint for a direct comparison. In addition, a visual overlay of specimen, colored in red, and visual hull, colored in blue, is given to highlight divergences. Areas where specimen and visual hull coincide are colored in purple. The view of the specimen and the 3D model chosen in the figure is representative of the 3D appearance of the visual hull. Based on the figure, it may become evident that the visual hull is a good approximation of the actual specimen. A detailed observation indicates that primarily the sharp-edged areas of the fracture edge have minimal deviations. These indications are confirmed by the evaluation with the μCT scanned specimens. With the help of this sophisticated but

Table 1: *Registration results. The columns R_{GT} and T_{GT} show the ground truth for the rendered specimens. The ground truth for T_z differs between the rendered specimens due to a vertical displacement of the break point images of 3D-skewed caused by the displaced specimen's tip. This displacement is taken into account in the ground truth data for 3D-skewed.*

Sampling	t	R_z	R_{GT}	T_z	T_{GT}	ε
3D						
$\theta_{step} = 10^\circ$	230	174.75°	175°	27	28	898.39
$\theta_{step} = 20^\circ$	219	174.51°	175°	28	28	1203.13
$\theta_{step} = 30^\circ$	210	174.51°	175°	28	28	1351.04
3D-skewed						
$\theta_{step} = 10^\circ$	221	174.51°	175°	13	21	2118.79
$\theta_{step} = 20^\circ$	215	174.26°	175°	16	21	2401.88
$\theta_{step} = 30^\circ$	206	174.26°	175°	14	21	2379.31
Real-1						
$\theta_{step} = 10^\circ$	212	2.35°	-	1	-	2658.36
$\theta_{step} = 20^\circ$	210	1.83°	-	6	-	2947.69
$\theta_{step} = 30^\circ$	205	359.09°	-	7	-	3155.65
Real-2						
$\theta_{step} = 10^\circ$	211	170.2°	-	-4	-	2731.18
$\theta_{step} = 20^\circ$	215	169.72°	-	-7	-	2947.02
$\theta_{step} = 30^\circ$	212	169.72°	-	-6	-	3257.36
Real-3						
$\theta_{step} = 10^\circ$	204	174.19°	-	64	-	2970.06
$\theta_{step} = 20^\circ$	205	168.39°	-	56	-	2979.62
$\theta_{step} = 30^\circ$	210	175.94°	-	63	-	3278.16
adjusted	-	180.87°	-	63	-	3443.7

(a) *Specimen* **(b)** *Visual Hull* **(c)** *Visual Overlay*

Figure 10: *Comparison of specimen and visual hull. (a) shows the steel specimen of the data set, (b) the 3D model of the visual hull and (c) the overlay of specimen (red) and visual hull (blue). The viewpoint for specimen and visual hull is identical.*

Table 2: *µCT and reconstruction comparison. Distances are denoted in* mm.

Specimen	Mean Distance	Standard Deviation
AMA55Z2$_{top}$	-0.0941	0.5415
AMA55Z2$_{bottom}$	-0.0662	0.0929
AMA55z3$_{top}$	-0.0827	0.1103
AMA55z3$_{bottom}$	-0.0993	0.4396
AMA55z262$_{top}$	-0.0128	0.0531
AMA55z262$_{bottom}$	0.0260	0.0586
AZK6z3$_{top}$	-0.0638	0.0138
AZK6z3$_{bottom}$	0.0112	0.2301

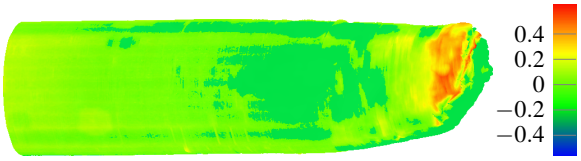

Figure 11: *Aligned µCT mesh with our reconstructed point cloud colored according to the Euclidean distance. Distances are in* mm.

expensive method, it is possible for us to gain access to a precise reconstruction and to compare our method with it. Table 2 shows our reconstruction result compared to the μCT data. To obtain this data, we manually aligned our generated point cloud with the CT-generated mesh. Afterwards, we densely sampled the CT mesh and applied the ICP algorithm with a fixed scale to align both sources as accurately as possible. The actual distances are then determined using the nearest neighbor distance (Euclidean distance). Beyond this, we have found that we get the most accurate results when we manually remove the edge of the break point, as this negatively affects the alignment process and does not reflect the precision of the overall specimen reconstruction. An example of the distances of the two aligned point clouds that illustrates this issues is shown in fig. 11. Overall, our results show a high precision and confirm the effectiveness of our reconstruction method.

Distance Measurement To study the material expansion during a fracture, the distance is required. Table 3 depicts the differences between the manual and our automatic method. The distance is obtained twice by measuring at two points, LA and LB. This invasive measurement method may cause material wear. Our method determines the distance based on the visible markers. The accuracy of our method is shown by the comparison with the non-fractured specimen. In this case, we measure the same distance in mm, accurate to two decimal digits. Despite having a noticeable difference between the manual and the automatic measurement of the reassembled specimens, both methods measure a similar distance. This deviation is justified by the fact that our method finds a near-optimal rotation and translation according to our experiments and that our pan angle alignment avoids any distance distortion bias, which occurs in manual measurements.

Table 3: *Distance measurements of two assembled and one non-fractured specimen. In the manual case, the two halves are pressed onto each other by eye.*

Specimen	Manual (LA)	Manual (LB)	Automatic (Ours)
Reassembled 1	51.8661 mm	51.8365 mm	52.4757 mm
Reassembled 2	50.2190 mm	50.1975 mm	51.1375 mm
Full	30.4125 mm	-	30.4114 mm

5. Conclusion and Future Work

The designing process of modern steel components with heat-resistant properties requires detailed knowledge of accurate material properties. We have identified two strategies to further improve the current approach, focusing on accuracy and robustness. First, we developed a novel post scan pan angle correction to diminish mechanical and human error sources. Second, we introduced a registration and reassembly algorithm for highly precise and robust fitting of broken specimen halves. This whole pipeline is non-invasive and inexpensive in comparison to μCT reconstructed specimen. Our results show that the mean deviation of our system is only 0.057 mm distributed over the whole specimen for sets of 36 images, which can be scanned in approximately five minutes. Furthermore, we are more robust, precise, and less error prone than current state-of-the-art microscopy measurements. We achieved this through a deterministic approach that is independent of human capabilities and counteracts past error sources. In future work, we want to expand our methods for a broader range of specimen shapes and generalize to a more scanning system independent approach.

Acknowledgements

We would like to thank the "Forschungsvereinigung der Arbeitsgemeinschaft der Eisen und Metall verarbeitenden Industrie e.V." (AVIF No. A314) for their financial support, working group "W13" of the "Forschungsvereinigung für warmfeste Stähle und Hochtemperaturwerkstoffe" for very fruitful discussions and the "Forschungsvereinigung für Verbrennungskraftmaschinen e.V." for accompanying the underlying research project. Part of the research in this paper was funded by the Deutsche Forschungsgemeinschaft (DFG, German Research Foundation) – project number 407714161. Additionally, we thank the anonymous reviewers whose comments helped improve this manuscript.

References

[AA20] AHARCHI, M. and AIT KBIR, M. "A Review on 3D Reconstruction Techniques from 2D Images". *Innovations in Smart Cities Applications Edition 3*. Springer International Publishing, 2020, 510–522. DOI: 10.1007/978-3-030-37629-1_37 2.

[AB83] ASHBY, M. and BROWN, L.M. *Perspectives in Creep Fracture*. Elsevier, 1983. DOI: 10.1016/c2013-0-06074-4 1, 2.

[AH03] ANDERSSON, TOMAS and HÄNDEL, PETER. "Standardized sine-wave fitting algorithms, extensions and applications". 2003 2, 3.

[Bau74] BAUMGART, BRUCE GUENTHER. *Geometric modeling for computer vision*. Stanford University, 1974 2.

[CBK04] CHEUNG, KONG-MAN (GERMAN), BAKER, SIMON, and KANADE, TAKEO. "Shape-From-Silhouette Across Time Part I: Theory and Algorithms". *International Journal of Computer Vision* 62.3 (Nov. 2004), 221–247. DOI: 10.1007/s11263-005-4881-5 2.

[EDDP20] ESLAMI, DARIUSH, DI ANGELO, LUCA, DI STEFANO, PAOLO, and PANE, CATERINA. "Review of computer-based methods for archaeological ceramic sherds reconstruction". *Virtual Archaeology Review* 11.23 (July 2020), 34. DOI: 10.4995/var.2020.13134 2.

[EHD00] ELGAMMAL, AHMED, HARWOOD, DAVID, and DAVIS, LARRY. "Non-parametric Model for Background Subtraction". *Lecture Notes in Computer Science*. Springer, 2000, 751–767. DOI: 10.1007/3-540-45053-x_48 2.

[Han00] HANDEL, P. "Properties of the IEEE-STD-1057 four-parameter sine wave fit algorithm". *IEEE Transactions on Instrumentation and Measurement* 49.6 (2000), 1189–1193. DOI: 10.1109/19.893254 2.

[KGK87] KLOOS, K. H., GRANACHER, J., and KOOY, A. "Kriech- und Bruchverhalten warmfester Stähle in kennzeichnenden Fällen veränderlicher Zeitstandbeanspruchung". *Materialwissenschaft und Werkstofftechnik* 18.11 (Nov. 1987), 381–390. DOI: 10.1002/mawe.19870181108 1.

[KS04] KAMPEL, M. and SABLATNIG, R. "On 3D mosaicing of rotationally symmetric ceramic fragments". *Proceedings of the 17th International Conference on Pattern Recognition, 2004. ICPR 2004.* Vol. 2. IEEE, 2004, 265–268. DOI: 10.1109/icpr.2004.1334157 2.

[KS99] KUTULAKOS, K.N. and SEITZ, S.M. "A theory of shape by space carving". *Proceedings of the Seventh IEEE International Conference on Computer Vision*. Vol. 2000. IEEE, 1999, 199–218. DOI: 10.1109/iccv.1999.791235 2, 4.

[KSK*07] KIM, HANSUNG, SAKAMOTO, RYUUKI, KITAHARA, ITARU, et al. "Robust Foreground Extraction Technique Using Gaussian Family Model and Multiple Thresholds". *Computer Vision – ACCV 2007*. Springer, 2007, 758–768. DOI: 10.1007/978-3-540-76386-4_72 2.

[KSK12] KIMURA, KAZUHIRO, SAWADA, KOTA, and KUSHIMA, HIDEAKI. "Creep Rupture Ductility of Creep Strength Enhanced Ferritic Steels". *Journal of Pressure Vessel Technology* 134.3 (May 2012). DOI: 10.1115/1.4005876 1.

[KSM05] KAMPEL, MARTIN, SABLATNIG, ROBERT, and MARA, HUBERT. *Robust 3D reconstruction of archaeological pottery based on concentric circular rills*. Vienna University of Technology, 2005 2.

[KvBG*21] KNAUTHE, VOLKER, von BUELOW, MAX, GUTHE, STEFAN, et al. "High precision orthographic specimen scanning system for the evaluation of creep rupture parameters". Langzeitverhalten warmfester Stähle und Hochtemperaturwerkstoffe. 44. Vortragsveranstaltung. Nov. 2021 2, 4.

[Lau94] LAURENTINI, A. "The visual hull concept for silhouette-based image understanding". *IEEE Transactions on Pattern Analysis and Machine Intelligence* 16.2 (1994), 150–162. DOI: 10.1109/34.273735 2, 4.

[LGZ20] LI, QUNHUI, GENG, GUOHUA, and ZHOU, MINGQUAN. "Pairwise Matching for 3D Fragment Reassembly Based on Boundary Curves and Concave-Convex Patches". *IEEE Access* 8 (2020), 6153–6161. DOI: 10.1109/access.2019.2961391 2.

[MBR*00] MATUSIK, WOJCIECH, BUEHLER, CHRIS, RASKAR, RAMESH, et al. "Image-based visual hulls". *Proceedings of the 27th annual conference on Computer graphics and interactive techniques - SIGGRAPH '00*. ACM Press, 2000, 369–374. DOI: 10.1145/344779.344951 2.

[McI00] MCIVOR, ALAN M. "Background subtraction techniques". *Proc. of Image and Vision Computing* 4 (2000), 3099–3104 2.

[MK03] MCBRIDE, JONAH C. and KIMIA, BENJAMIN B. "Archaeological Fragment Reconstruction Using Curve-Matching". *2003 Conference on Computer Vision and Pattern Recognition Workshop*. Vol. 1. IEEE, June 2003, 3–3. DOI: 10.1109/cvprw.2003.10008 2.

[MYA03] MULAYIM, A.Y., YILMAZ, U., and ATALAY, V. "Silhouette-based 3-D model reconstruction from multiple images". *IEEE Transactions on Systems, Man and Cybernetics, Part B (Cybernetics)* 33.4 (Aug. 2003), 582–591. DOI: 10.1109/tsmcb.2003.814303 2.

[Pic04] PICCARDI, M. "Background subtraction techniques: a review". *2004 IEEE International Conference on Systems, Man and Cybernetics (IEEE Cat. No.04CH37583)*. Vol. 4. IEEE, 2004, 3099–3104. DOI: 10.1109/icsmc.2004.1400815 2.

[PJ17] PAULANO-GODINO, FÉLIX and JIMÉNEZ-DELGADO, JUAN J. "Identification of fracture zones and its application in automatic bone fracture reduction". *Computer Methods and Programs in Biomedicine* 141 (Apr. 2017), 93–104. DOI: 10.1016/j.cmpb.2016.12.014 2.

[PK03] PAPAIOANNOU, GEORGIOS and KARABASSI, EVAGGELIA-AGGELIKI. "On the automatic assemblage of arbitrary broken solid artefacts". *Image and Vision Computing* 21.5 (May 2003), 401–412. DOI: 10.1016/s0262-8856(03)00008-8 2.

[RN14] RASHEED, NADA A. and NORDIN, MD JAN. "A POLYNOMIAL FUNCTION IN THE AUTOMATIC RECONSTRUCTION OF FRAGMENTED OBJECTS". *Journal of Computer Science* 10.11 (Nov. 2014), 2339–2348. DOI: 10.3844/jcssp.2014.2339.2348 2.

[Sak19] SAKPERE, WILSON. "3D Reconstruction of Archaeological Pottery from Its Point Cloud". *Pattern Recognition and Image Analysis*. Springer International Publishing, 2019, 125–136. DOI: 10.1007/978-3-030-31332-6_11 2.

[SAT06] SHIMADA, ATSUSHI, ARITA, DAISAKU, and TANIGUCHI, RIN-ICHIRO. "Dynamic Control of Adaptive Mixture-of-Gaussians Background Model". *2006 IEEE International Conference on Video and Signal Based Surveillance*. IEEE, Nov. 2006, 5–5. DOI: 10.1109/avss.2006.44 2.

[Sch21] SCHNEIDER, DAVID C. "Visual hull". *Computer Vision: A Reference Guide*. Springer, 2021, 1363–1366. DOI: 10.1007/978-0-387-31439-6 2.

[SLLL17] SON, TAE-GEUN, LEE, JUSUNG, LIM, JEONGHUN, and LEE, KUNWOO. "Reassembly of fractured objects using surface signature". *The Visual Computer* 34.10 (July 2017), 1371–1381. DOI: 10.1007/s00371-017-1419-0 2.

[Wan19] WANG, CHEN. "Kernel learning for visual perception". PhD thesis. 2019, 17. DOI: 10.32657/10220/47835 4.

[WC04] WILLIS, A.R. and COOPER, D.B. "Bayesian assembly of 3D axially symmetric shapes from fragments". *Proceedings of the 2004 IEEE Computer Society Conference on Computer Vision and Pattern Recognition, 2004. CVPR 2004.* Vol. 1. IEEE, 2004. DOI: 10.1109/cvpr.2004.1315017 2.

[WWAG88] WOOD, D. S., WYNN, J., AUSTIN, C., and GREEN, J. G. "A DUCTILITY EXHAUSTION EVALUATION OF SOME LONG TERM CREEP/FATIGUE TESTS ON AUSTENITIC STEEL". *Fatigue & Fracture of Engineering Materials and Structures* 11.5 (Sept. 1988), 371–381. DOI: 10.1111/j.1460-2695.1988.tb01390.x 1.

[ZYM*15] ZHANG, KANG, YU, WUYI, MANHEIN, MARY, et al. "3D Fragment Reassembly Using Integrated Template Guidance and Fracture-Region Matching". *2015 IEEE International Conference on Computer Vision (ICCV)*. IEEE, Dec. 2015, 2138–2146. DOI: 10.1109/iccv.2015.247 2.